EUROPEAN ORGANISATION FOR NUCLEAR RESEARCH (CERN)

Submitted to: JHEP

CERN-EP-2022-130
26th July 2022

Exclusive dielectron production in ultraperipheral Pb+Pb collisions at $\sqrt{s_{\mathrm{NN}}} = 5.02$ TeV with ATLAS

The ATLAS Collaboration

Exclusive production of dielectron pairs, $\gamma\gamma \to e^+e^-$, is studied using $\mathcal{L}_{\mathrm{int}} = 1.72$ nb^{-1} of data from ultraperipheral collisions of lead nuclei at $\sqrt{s_{\mathrm{NN}}} = 5.02$ TeV recorded by the ATLAS detector at the LHC. The process of interest proceeds via photon–photon interactions in the strong electromagnetic fields of relativistic lead nuclei. Dielectron production is measured in the fiducial region defined by following requirements: electron transverse momentum $p_{\mathrm{T}}^{e} > 2.5$ GeV, absolute electron pseudorapidity $|\eta^{e}| < 2.5$, dielectron invariant mass $m_{ee} > 5$ GeV, and dielectron transverse momentum $p_{\mathrm{T}}^{ee} < 2$ GeV. Differential cross-sections are measured as a function of m_{ee}, average p_{T}^{e}, absolute dielectron rapidity $|y_{ee}|$, and scattering angle in the dielectron rest frame, $|\cos\theta^{*}|$, in the inclusive sample, and also with a requirement of no activity in the forward direction. The total integrated fiducial cross-section is measured to be $215 \pm 1(\mathrm{stat.})\,^{+23}_{-20}(\mathrm{syst.}) \pm 4(\mathrm{lumi.})\ \mu$b. Within experimental uncertainties the measured integrated cross-section is in good agreement with the QED predictions from the Monte Carlo programs Starlight and SuperChic, confirming the broad features of the initial photon fluxes. The differential cross-sections show systematic differences from these predictions which are more pronounced at high $|y_{ee}|$ and $|\cos\theta^{*}|$ values.

Contents

1 Introduction

Collisions of ultrarelativistic heavy ions provide an opportunity to study not only the strong interactions between nucleons but also processes involving electromagnetic (EM) interactions. This is due to the presence of intense EM fields associated with the ultrarelativistic ions. The EM interactions become dominant at large impact parameters, $b > 2R_A$, where R_A is the ion radius. Such collisions are usually referred to as ultraperipheral collisions (UPC). Comprehensive reviews of UPC physics can be found in Refs. [1, 2].

The EM fields associated with the ultrarelativistic nuclei can be treated as fluxes of quasi-real photons according to the equivalent photon approximation (EPA) formalism [3, 4]. In this approach, the total cross-section for a given process is calculated as a convolution of the photon flux with the elementary production cross-section. Although the same approach is also valid for proton–proton (pp) collisions, the expected cross-sections are strongly enhanced in the heavy-ion (HI) collisions. The photon flux from each nucleus is enhanced by a factor of Z^2, where Z is the atomic number. That results in a Z^4 enhancement of the cross-sections. For lead (Pb, $Z = 82$), this Z^4 enhancement is 4.5×10^7. Another advantage of studying photon-induced interactions in UPC HI collisions is the relatively low number of interactions per LHC bunch crossing. The mean number of simultaneous interactions, μ, is typically at the subpercent level. This provides a clean environment, facilitating the detection of the interaction products, and little contamination from unrelated interactions in the same crossing. With the centre-of-mass energy per nucleon pair available at the Large Hadron Collider (LHC), $\sqrt{s_{\mathrm{NN}}} = 5.02\,\mathrm{TeV}$, the initial photons can reach energies up to 75–100 GeV.

Among the possible set of photon-induced reactions, the exclusive production of dielectron pairs from photon–photon collisions, i.e. $\gamma\gamma \to e^+e^-$, is one of the cleanest elementary processes. This process, also referred to as the Breit–Wheeler process [5], is a non-resonant two-photon scattering to opposite-charge electron pairs. The outgoing nuclei may be excited, for example via the giant dipole resonance [6]. A

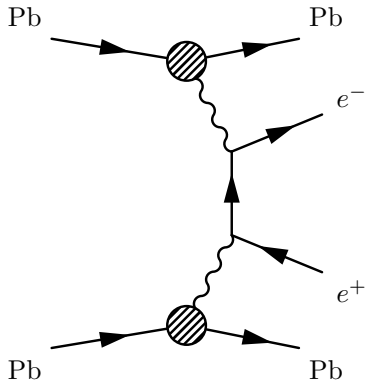

Figure 1: Feynman diagram of the leading-order $\gamma\gamma \to e^+e^-$ process.

Feynman diagram of the leading-order $\gamma\gamma \to e^+e^-$ reaction is shown in Figure 1. Even for large $\gamma\gamma$ invariant masses, the relatively large cross-section associated with this process allows precise differential measurements to be made. Thus, this process is a particularly effective tool for studying the modelling of photon fluxes and elementary production cross-sections, as well as for studying the effects of nuclear break-up, whose probability is strongly correlated with the internuclear impact parameter [2]. Nuclear break-up gives rise to forward neutron production, and the fraction of events with such activity is larger at smaller impact parameters.

Exclusive dilepton production, via both electron-pair and muon-pair final states, has been measured by ATLAS and CMS in pp collisions at $\sqrt{s} = 7$ TeV [7–9] and $\sqrt{s} = 13$ TeV [10–12]. The ALICE Collaboration has measured exclusive production of electron pairs in Pb+Pb collisions at $\sqrt{s_{\mathrm{NN}}} = 2.76$ TeV [13] over a limited kinematic range. The STAR experiment at RHIC has measured exclusive dileptons at lower invariant masses at $\sqrt{s_{\mathrm{NN}}} = 200$ GeVfor both Au+Au and U+U collisions [14, 15]. With the higher centre-of-mass energy of $\sqrt{s_{\mathrm{NN}}} = 5.02$ TeV, ATLAS has performed differential measurements of $\gamma\gamma \to \mu^+\mu^-$ production in UPC Pb+Pb collisions [16]. Both STAR and ATLAS have observed substantial broadening of angular distributions for exclusive dileptons from $\gamma\gamma$ interactions in events where the nuclei overlapped and interacted hadronically [14, 17]. Finally, CMS has observed that angular correlations in exclusive dimuon events are broadened significantly as a function of the impact parameter [18], as inferred by the amount of forward neutron production.

Exclusive dielectron production is an important reference process for other measurements. References [19] and [20] propose using it in the context of $\gamma\gamma \to \tau^+\tau^-$ production, in order to reduce the impact of correlated systematic uncertainties for the measurement of the τ-lepton anomalous magnetic moment. It is also an important background for light-by-light scattering, which proceeds via loop diagrams and thus has a much lower cross-section. This has been assessed in several publications on light-by-light scattering by ATLAS [21–23] and CMS [24].

This paper presents a measurement of the exclusive production of dielectrons with the ATLAS detector at the LHC. It uses Pb+Pb data collected in 2018, which have an integrated luminosity three times larger than the sample used in the ATLAS dimuon measurement [16]. Dielectron production is measured in the fiducial region defined by the following requirements: electron transverse momentum $p_{\mathrm{T}}^{e} > 2.5$ GeV, electron pseudorapidity $|\eta^{e}| < 2.5$, dielectron invariant mass $m_{ee} > 5$ GeV, and dielectron transverse momentum $p_{\mathrm{T}}^{ee} < 2$ GeV. Compared to the dimuon measurement discussed in Ref. [16], this fiducial region has wider coverage in lepton p_{T} and dilepton invariant mass, with the minimum values lowered by

1.5 GeV and 5 GeV, respectively. The backgrounds originating from single-dissociative processes, $\Upsilon(nS)$ production, and exclusive τ-lepton pair production, $\gamma\gamma \to \tau^+\tau^-$, are estimated and subtracted. Differential cross-sections are measured as a function of m_{ee}, average electron transverse momentum $\langle p_{\mathrm{T}}^e \rangle$, absolute dielectron rapidity $|y_{ee}|$, and scattering angle in the dielectron rest frame, $|\cos\theta^*|$. The cross-sections are extracted both inclusively in forward neutron activity and exclusively in $\gamma\gamma \to e^+e^-$ events without activity in the forward direction. The latter is a unique feature of this paper.

2 ATLAS detector

The ATLAS detector [25] at the LHC covers nearly the entire solid angle around the collision point. It consists of an inner tracking detector surrounded by a thin superconducting solenoid, electromagnetic and hadronic calorimeters, and a muon spectrometer incorporating three large superconducting toroidal magnets with eight coils each.

The inner detector (ID) is immersed in a 2 T axial magnetic field and provides charged-particle tracking in the pseudorapidity range $|\eta| < 2.5$.[1] The high-granularity silicon pixel (Pixel) detector covers the vertex region and typically provides four measurements per track, with the first hit normally being in the insertable B-layer (IBL) [26], which was installed at the mean distance of 3.3 cm from the beam axis before the start of Run 2. It is followed by the silicon microstrip tracker (SCT), which usually provides four two-dimensional measurement points per track. These silicon detectors are complemented by the transition radiation tracker, which enables radially extended track reconstruction up to $|\eta| = 2.0$.

The calorimeter system covers the pseudorapidity range $|\eta| < 4.9$. Within the region $|\eta| < 3.2$, electromagnetic calorimetry is provided by barrel and endcap lead/liquid-argon (LAr) calorimeters (high granularity for $|\eta| < 2.5$), with an additional thin LAr presampler covering $|\eta| < 1.8$ to correct for energy loss in material upstream of the calorimeters. Hadronic calorimetry is provided by the steel/scintillator-tile calorimeter, which is segmented into three barrel structures within $|\eta| < 1.7$, and two copper/LAr hadronic endcap calorimeters. The solid angle coverage is completed with forward copper/LAr and tungsten/LAr calorimeter modules (FCal) optimised for electromagnetic and hadronic measurements respectively.

The muon spectrometer (MS) comprises separate trigger and high-precision tracking chambers measuring the deflection of muons in a magnetic field generated by the superconducting air-core toroids. The precision chamber system covers the region $|\eta| < 2.7$ with three layers of monitored drift tubes, complemented by cathode strip chambers in the forward region, where the background is highest. The muon trigger system covers the range $|\eta| < 2.4$ with resistive plate chambers in the barrel, and thin gap chambers in the endcap regions.

The zero-degree calorimeters (ZDC) consist of four longitudinal compartments on each side of the IP, each with one nuclear interaction length of tungsten absorber, with Cherenkov light read out by 1.5-mm-diameter quartz rods. The detectors are located 140 m from the nominal IP in both directions, covering $|\eta| > 8.3$, and are well suited to measuring neutral particles originating from the collision. In Pb+Pb collisions the ZDC detects individual neutrons originating from the incoming nuclei. The ZDC calibration is performed

[1] ATLAS uses a right-handed coordinate system with its origin at the nominal interaction point (IP) in the centre of the detector and the z-axis along the beam pipe. The x-axis points from the IP to the centre of the LHC ring, and the y-axis points upwards. Cylindrical coordinates (r, ϕ) are used in the transverse plane, ϕ being the azimuthal angle around the z-axis. The pseudorapidity is defined in terms of the polar angle θ as $\eta = -\ln\tan(\theta/2)$. Angular distance is measured in units of $\Delta R \equiv \sqrt{(\Delta\eta)^2 + (\Delta\phi)^2}$. The photon (electron) transverse energy is $E_{\mathrm{T}} = E/\cosh(\eta)$, where E is its energy.

in each set of four modules using photonuclear processes that deposit one or more neutrons on one side, and a single neutron, carrying the full per-nucleon beam energy, on the other. Time-dependent weights are determined for each module in short time intervals to minimise the variance around the nominal per-nucleon beam energy. Energy resolutions achieved are typically around $\Delta E/E \approx 16\%$.

The ATLAS trigger system [27, 28] consists of a first-level (L1) trigger implemented using a combination of dedicated electronics and programmable logic, and a software-based high-level trigger (HLT). An extensive software suite [29] is used in the reconstruction and analysis of real and simulated data, in detector operations, and in the trigger and data acquisition systems of the experiment.

3 Data and Monte Carlo simulation samples

The data used in this measurement are from Pb+Pb collisions with a centre-of-mass energy of $\sqrt{s_{\mathrm{NN}}} = 5.02\,\mathrm{TeV}$, recorded in 2018 with the ATLAS detector at the LHC. The full data set corresponds to an integrated luminosity of $1.72\,\mathrm{nb}^{-1}$. Only high-quality data [30] with all detectors operating normally are analysed.

Monte Carlo (MC) simulated events for the $\gamma\gamma \to e^+e^-$ signal process were generated at leading order (LO) using Starlight v3.13 [31]. In this approach, the cross-section is computed by convolving the Pb+Pb photon flux with the LO calculation of the elementary $\gamma\gamma \to e^+e^-$ process. The photon spectrum is calculated in impact parameter space by integrating the photon number density over all impact parameters while assuming that the beam projectiles do not interact hadronically. This is done by utilising a simple Glauber model [32] which provides an impact-parameter-dependent probability of inelastic processes. Starlight also requires that the dilepton pairs are not formed within either nucleus. Several signal samples were produced for exclusive m_{ee} intervals within the range $4.5 < m_{ee} < 200\,\mathrm{GeV}$. An alternative sample for the signal $\gamma\gamma \to e^+e^-$ process uses the SuperChic v3.05 [33] program. The difference between the nominal and alternative signal prediction is mainly in the implementation of the non-hadronic overlap condition of the Pb ions. In SuperChic the probability for exclusive $\gamma\gamma \to e^+e^-$ interactions turns on smoothly for Pb+Pb impact parameters in the range of 15–20 fm and it is unity for larger values.

Backgrounds from $\gamma\gamma \to \tau^+\tau^-$ and $\Upsilon(nS) \to e^+e^-$ were simulated using Starlight v3.13. All generated events utilised Pythia 8 (Py8) [34] to model QED final-state radiation (FSR) from the outgoing leptons.

Background contributions from exclusive dielectron production where either one (single dissociation) or both (double dissociation) nuclei interact inelastically and dissociate were modelled using SuperChic v4.0 (SC4) [35]. It was interfaced to Pythia 8 for showering and hadronisation. Since simulation of this process is only available for pp collisions, a data-driven approach, discussed in detail in Section 5, is used in the analysis to utilise this sample in Pb+Pb collisions.

Apart from the alternative signal sample, all generated events are processed with a detector simulation [36] based on Geant4 [37] and are reconstructed with the standard ATLAS reconstruction software [29]. The alternative signal sample is used for comparisons with the measured differential cross-sections discussed in Section 8.

4 Signal selection and detector corrections

Candidate dielectron events were recorded using a dedicated trigger for events with moderate activity in the calorimeter but little additional activity in the entire detector. A logical OR of two L1 trigger conditions was required: (1) at least one EM cluster with $E_{\mathrm{T}} > 1$ GeV in coincidence with a total E_{T} of 4–200 GeV registered in the calorimeter, or (2) at least two EM clusters with $E_{\mathrm{T}} > 1$ GeV and a total E_{T} below 50 GeV registered in the calorimeter. At the HLT, the total E_{T} on each side of the FCal detector was required to be below 3 GeV. Additionally, a veto condition on the maximum activity in the Pixel detector, hereafter referred to as the Pixel-veto, had to be satisfied at the HLT. The number of hits was required to be at most 15 to be compatible with low-multiplicity UPC events.

Electrons are reconstructed from EM clusters in the calorimeter and tracking information provided by the ID [38]. Selection requirements are applied to remove EM clusters with a large amount of energy from poorly functioning calorimeter cells, and a timing requirement is made to reject out-of-time candidates. An energy calibration specifically optimised for electrons and photons [38] is applied to the candidates to account for upstream energy loss and both lateral and longitudinal shower leakage. The calibration is derived for nominal pp collisions with dedicated factors applied to account for the much lower contribution from multiple Pb+Pb collisions in the same bunch crossing.

The electron identification in this analysis is based on a 'loose' cut-based working point [38] which is defined using selections on the shower-shape and tracking variables. Only electrons with $p_{\mathrm{T}}^{e} > 2.5$ GeV and $|\eta^{e}| < 2.47$, excluding the calorimeter transition region $1.37 < |\eta^{e}| < 1.52$, are considered. The minimum p_{T}^{e} requirement is driven by the electron reconstruction efficiency, which drops below 20% for p_{T}^{e} values below this threshold.

Preselected events are required to have exactly two opposite-charge electrons satisfying the above selection criteria, with a dielectron invariant mass, m_{ee}, greater than 5 GeV. To suppress non-exclusive backgrounds, only two charged-particle tracks [39, 40] each with $p_{\mathrm{T}} > 100$ MeV, $|\eta| < 2.5$, at least seven hits in the Pixel and SCT detectors in total and at most two silicon sensors without a hit, and associated with the dielectron are allowed. To reject non-collision backgrounds such as cosmic-ray muons, the event must not have a track in the MS. Finally, the total p_{T} of the dielectron, p_{T}^{ee}, is required to be less than 2 GeV. Low p_{T}^{ee} values are a key feature of the purely EM process, which involves initial-state photons with very low p_{T}.

Each of the events satisfying the $\gamma\gamma \to e^{+}e^{-}$ criteria can be further classified into one of three categories based on the observed activity in the ZDC detector: 1) no neutron is registered in either ZDC ('0n0n'), 2) one or more forward neutrons registered in one ZDC and none in the other ('Xn0n'), and 3) one or more forward neutrons detected in both ZDC arms ('XnXn'). The observed fractions of events falling into these categories are: $f_{\mathrm{0n0n}} = (62.9 \pm 0.3)\%$, $f_{\mathrm{Xn0n}} = (29.7 \pm 0.3)\%$, and $f_{\mathrm{XnXn}} = (7.4 \pm 0.2)\%$. Due to the relatively large instantaneous luminosity of Pb+Pb collisions, which peaked around $7 \times 10^{27}\,\mathrm{cm}^{-2}\mathrm{s}^{-1}$, additional neutrons might be generated per bunch crossing and detected in one or both arms of the ZDC, but they are not associated with the exclusive dielectron process. This leads to an outflow of events from the 0n0n and Xn0n categories to both the Xn0n and XnXn categories. This effect is accounted for using the method established in Ref. [16]. A matrix equation with two fundamental parameters representing probabilities for having additional neutrons in one or both arms of the ZDC is built. The corrected fractions are measured in four bins of m_{ee}, with boundaries at 5, 10, 20, and 40 GeV, and three bins of $|y_{ee}|$, with boundaries at 0, 0.8, 1.6, and 2.4, and also in the sample integrated over m_{ee} and $|y_{ee}|$. On average, they are about 13% larger than the observed fractions. Figure 2 shows the fractions of events in the 0n0n category as a function of m_{ee} in three bins of $|y_{ee}|$, corrected for the presence of additional neutrons.

These fractions tend to drop with increasing mass, and are in general larger for higher $|y_{ee}|$ values. For the rapidity range of $|y_{ee}| < 0.8$, which has the largest number of events, the f_{0n0n} values drop from about 78% in the lowest mass bin to about 57% in the highest mass bin. The systematic uncertainties in the fractions of events in the 0n0n category originate from several sources: uncertainties in the exclusive single and double EM dissociation probabilities measured by the ALICE Collaboration [41], and their extrapolation from $\sqrt{s_{\mathrm{NN}}} = 2.76$ TeV to 5.02 TeV as evaluated in Ref. [16]; the uncertainty in the dissociative background contribution as discussed in Section 5; and the uncertainty in the ZDC efficiency.

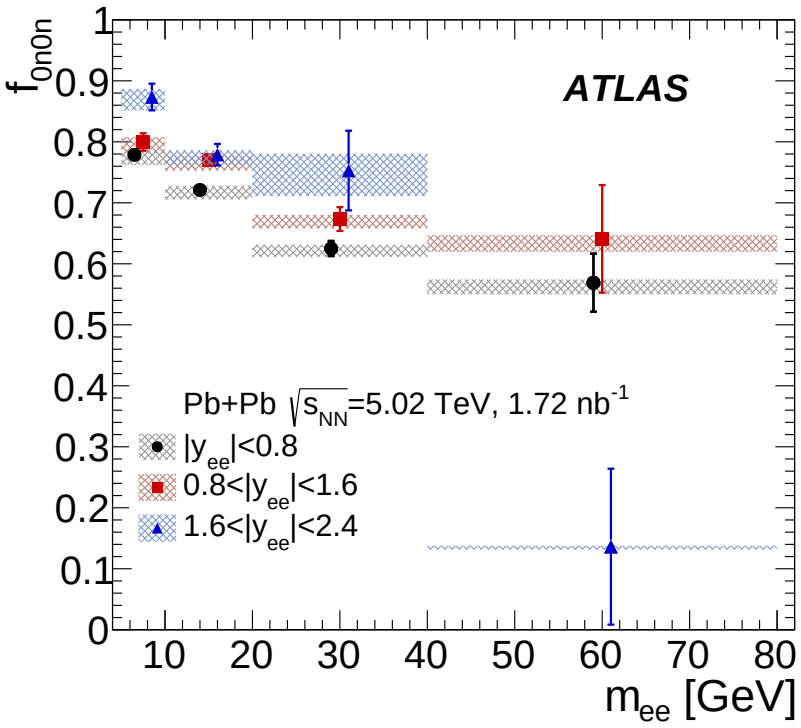

Figure 2: Fractions of events in the 0n0n category evaluated from data in three bins of $|y_{ee}|$, corrected for the presence of additional neutrons. Error bars represent statistical uncertainties, while shaded boxes represent systematic uncertainties. Points for $|y_{ee}| < 0.8$ and $1.6 < |y_{ee}| < 2.4$ are displaced horizontally for better visibility.

The efficiency of the primary physics trigger (ϵ_{T}) is determined as $\epsilon_{\mathrm{T}} = \varepsilon_{\mathrm{L1}} \cdot \varepsilon_{\mathrm{PixVeto}} \cdot \varepsilon_{\mathrm{FCal}}$, where $\varepsilon_{\mathrm{L1}}$ is the efficiency of the L1 EM trigger to register the moderate calorimeter activity characteristic of the signal process, $\varepsilon_{\mathrm{PixVeto}}$ is the efficiency of the trigger to reject events with large numbers of Pixel detector hits, and $\varepsilon_{\mathrm{FCal}}$ is the efficiency of the FCal selection to reject events with large energy depositions on either side. Individual efficiencies are evaluated in a sample of $\gamma\gamma \to e^+e^-$ events collected with a set of dedicated supporting triggers that do not use the condition under study in the primary physics trigger to reject any events. The $\varepsilon_{\mathrm{L1}}$ value rises with the sum of the transverse energies of the two electron clusters and reaches 100% for $\Sigma E_{\mathrm{T}} > 8$ GeV. The Pixel-veto efficiency is measured as a function of the dielectron rapidity; it is just over 80% for $|y_{ee}| \sim 0$ and falls to about 50% for $|y_{ee}| > 2$. The dependence on $|y_{ee}|$ originates from the growing number of Pixel-detector layers in the forward direction that a dielectron pair has to pass through. Finally, the FCal veto efficiency is measured to be (99.1 ± 0.6)%, and it is constant for the entire

range in ΣE_{T}. The total uncertainty in the trigger efficiency is determined by increasing and decreasing all of the individual components by their respective total uncertainties. They amount to about 3%–4% for the primary calorimeter pair trigger, driven mainly by the limited number of dielectron events collected by an independent ZDC-based trigger used to measure $\varepsilon_{\mathrm{L1}}$, and less than a percent for the other contributions.

The total electron efficiency is the product of the electron reconstruction efficiency and the 'loose' electron identification efficiency [38]. This is determined in data using a sample of events triggered by the presence of EM clusters, limited total E_{T}, and a maximal number of Pixel hits, on which a tag-and-probe procedure is performed. The tag is a well-reconstructed, high-purity electron candidate with $E_{\mathrm{T}} > 2.5\,\mathrm{GeV}$, and the probe is an opposite-charge track built from at least three hits in the Pixel detector (referred to as a 'Pixel-track'). The invariant mass of the tag-and-probe system must exceed 5 GeV and the acoplanarity ($\alpha = 1 - |\Delta\phi|/\pi$, where $\Delta\phi$ is the azimuthal angle between the two electrons) has to be less than 0.1. The extracted mass distribution is found to agree well with a reconstructed sample of Starlight events. The reconstruction efficiency is defined as the fraction of probes which are reconstructed electrons, while the identification efficiency is the fraction of reconstructed electrons which are identified as 'loose' electrons. The reconstruction efficiency has large variations with both p_{T} and Pixel-track η, and ranges from about 30% at $p_{\mathrm{T}} = 2.5\,\mathrm{GeV}$ to 95% above 15 GeV. The identification efficiency is found to vary more weakly with Pixel-track η, ranging between 80% and 90%. Then, the overall reconstruction scale factors are extracted as the ratio of efficiencies measured in data and MC simulation. They vary between 0.9 and 1.2, with the largest deviations from unity being in the forward direction for Pixel-track $|\eta| > 1.1$. Systematic uncertainties in the scale factors are evaluated using tighter selection criteria for the tag and probe candidates, as well as reducing a potential contribution from background processes by limiting the measurement to the 0n0n category or to a narrow acoplanarity region, $\alpha < 0.01$. The total systematic uncertainty is at the level of 5% for central Pixel-tracks with $|\eta| < 1$, and grows to 10% in the forward direction. In the forward region, the statistical and systematic uncertainties are of similar size.

5 Background contributions

There are three primary sources of background considered in this analysis, presented in order of decreasing contributions: dissociative electron-pair production where one or both photons are emitted from a resolved nucleon, and not coherently from the whole nucleus; Υ-meson production; and exclusive τ-lepton pair ($\tau^+\tau^-$) production.

The largest background originates from $\gamma\gamma \to e^+e^-$ production with nuclear dissociation. In this process one (or both) of the initial photons originates from the substructure of the nucleon, rather than from the exterior EM field of the nuclei as a whole. The photon interaction that produces the e^+e^- pair is thus accompanied by the dissociation of the emitting nucleus, whose remnants are produced in the forward direction and are typically captured by the ZDC detector.

The contribution from dissociative events is estimated using a template-fitting approach applied to the acoplanarity distribution. The signal template is simulated with Starlight + Pythia 8 and it is peaked at $\alpha \approx 0$, with some contribution in the tail originating from events with FSR. The background template shape is taken from the single-dissociative events simulated in pp collisions with SuperChic v4.0 interfaced with Pythia 8. These events have a much wider α distribution than the signal. The acoplanarity shape is strongly correlated with the transverse momentum of the $\gamma\gamma$ system, which is driven by the transverse momenta of the initial photons. For the photons emitted coherently from the nucleus, the transverse momentum is of order $\hbar c/R_A \approx 30\,\mathrm{MeV}$, while typical p_{T} scale for dissociative events is of order GeV. In the case

of dilepton production in pp collisions, the typical initial p_{T} scale is about 200 MeV. The convolution of photon fluxes originating from either proton or ion with photons emitted from nucleon substructure is always dominated by the harder spectrum of the latter. Therefore, the shape of the acoplanarity distribution for dissociative dielectron production in Pb+Pb collisions can be described by the simulation of this process in pp collisions. The fit to the data is performed in the same intervals of m_{ee} and $|y_{ee}|$ as in the study of the fractions of events in the 0n0n, Xn0n and XnXn categories. In each bin, a binned maximum-likelihood fitting procedure is performed separately in three ZDC categories. The normalisation of the relative background contribution, f_{bkg}, is taken to be a free parameter of the fit. The signal fraction is thus $(1 - f_{\mathrm{bkg}})$. For the inclusive sample, f_{bkg} is a weighted sum of the results for the 0n0n, Xn0n, and XnXn categories. The f_{bkg} fraction accounts for contributions from dissociative production and exclusive $\tau^+\tau^-$ production, $\gamma\gamma \to \tau^+\tau^-$. The latter may contribute to the electron background, especially when both τ-leptons decay in the electron channel. The $\tau^+\tau^-$ contribution is estimated using a dedicated MC sample from Starlight. The resulting background fraction of $\gamma\gamma \to \tau^+\tau^-$ events in the full data sample amounts to 0.1%. It is found that the shape of the α distribution for the exclusive $\tau^+\tau^-$ events is similar to the α distribution for the pure dissociative component. However, the origin of this shape in $\tau^+\tau^-$ events is due to the presence of the neutrino in τ-lepton decay. The dissociative contribution, f_{diss}, is therefore determined as the background fraction obtained from the fitting procedure, then reduced by the $\tau^+\tau^-$ background fraction.

The results of the fitting procedure for the data from the $10 < m_{ee} < 20\,\mathrm{GeV}$ and $|y_{ee}| < 0.8$ interval are presented in Figure 3 for three ZDC categories as well as for the inclusive sample. The f_{bkg} fraction amounts to $(0.3 \pm 0.2)\%$, $(9.9 \pm 0.6)\%$, $(13 \pm 1)\%$ and $(4.3 \pm 0.3)\%$ for the 0n0n, Xn0n, XnXn categories, and the inclusive sample, respectively.

The contribution from Υ-meson production is estimated using the dedicated Starlight + Pythia 8 samples. Three Υ states, $\Upsilon(1S)$, $\Upsilon(2S)$, and $\Upsilon(3S)$ are considered. This background is significant only for m_{ee} below 14 GeV and amounts to 2.4% of events satisfying the selection criteria for the $\gamma\gamma \to e^+e^-$ process. The α distribution of the dielectron candidates from Υ decays is peaked at zero, similarly to the signal shape. It does not contribute to f_{bkg} because the resulting fraction is not sensitive to a 2.4% change in the acoplanarity peak. Hence, the Υ contribution is subtracted separately from the data.

A background contribution originating from photonuclear processes occurring in peripheral heavy-ion collisions is largely suppressed by the trigger requirement limiting the maximum E_{T} deposited in the FCal to 3 GeV per side. The validity of this assumption was tested by examining the multiplicity distribution of Pixel-tracks. The fraction of events that have more than two Pixel-tracks is 1.3% and consistent with simulations of $\gamma\gamma \to e^+e^-$ events.

Figure 4 shows control distributions for reconstructed and uncorrected values of m_{ee}, $\langle p_{\mathrm{T}}^e \rangle$, y_{ee}, $|\cos\theta^*| = |\tanh(\Delta\eta_{ee}/2)|$, and α for the inclusive data sample compared with MC predictions including the signal and background processes. The trigger decision is not simulated in the MC events. Instead, the distributions are weighted event-by-event by the parameterised trigger efficiency and by electron scale factors. The signal, Υ decay and $\tau^+\tau^-$ MC prediction is normalised to the integrated luminosity in data. The dissociative contribution is scaled to constitute the f_{diss} fraction (determined for the inclusive sample) of the data. In general, good agreement between data and the sum of the predictions for signal and background processes is found. On average, the observed discrepancies are at the level of 10%–15% with some exceptions which are discussed further. In the m_{ee} distribution the data excess is more strongly pronounced for m_{ee} between 10 and 20 GeV, where the difference between data and MC simulation is 10%–20%. The data-to-MC ratio drops below unity for masses above 40 GeV. The same features are observed in the $\langle p_{\mathrm{T}}^e \rangle$ distribution, with the largest deviations from unity in the range 5–10 GeV. In the y_{ee} distribution, the data excess is smaller, up to 10%, in the range from -1.2 to 1.2, with larger discrepancies for higher $|y_{ee}|$ values. The data-to-MC

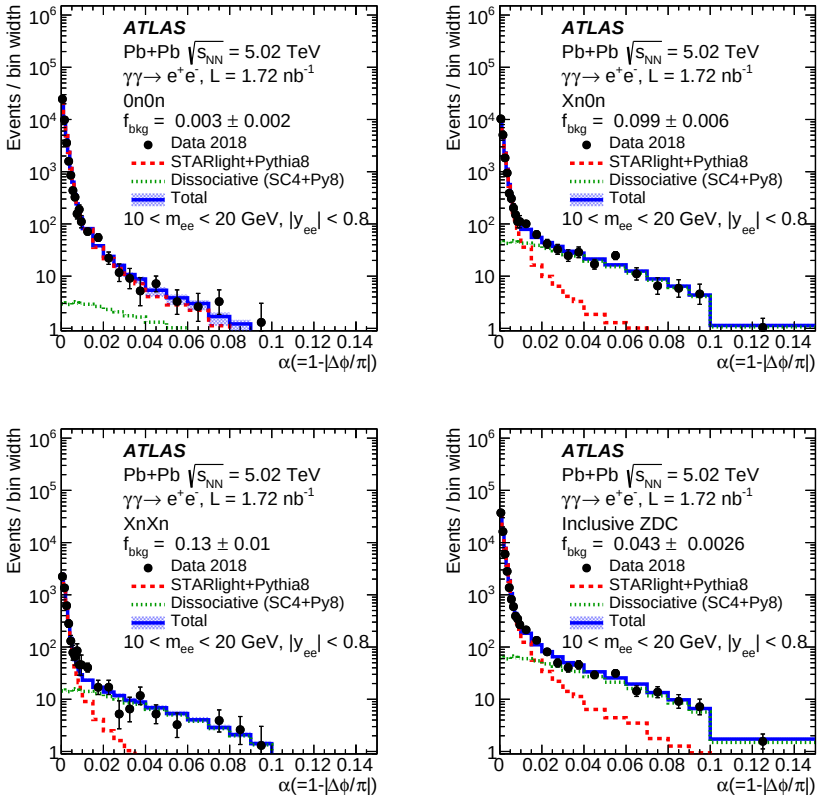

Figure 3: Acoplanarity distribution in the data sample (markers) of $\gamma\gamma \to e^+e^-$ candidates selected with $10 < m_{ee} < 20\,\text{GeV}$ and $|y_{ee}| < 0.8$ requirements. The sample is split into 0n0n (top left), Xn0n (top right), XnXn (bottom left) and inclusive (bottom right) categories. The fitted dissociative background in each category is shown with the green dashed line, while the prediction for the signal process is shown by the red line. The sum of the two components is shown with the solid blue line. The resulting estimate of the background fraction in the data, f_{bkg}, is given in the legend. The shaded area represents the total uncertainty of the sum of signal and background components.

ratio in the $|\cos\theta^*|$ distribution drops slowly from 1.2 for $|\cos\theta^*| = 0$ to unity at $|\cos\theta^*| = 0.75$, and then falls more steeply, to 0.5 for the largest values of $|\cos\theta^*|$. In the α distribution, a difference in the overall shape is observed in the full range. This can be explained by a sensitivity of the results to the p_{T} spectrum assumed by STARLIGHT, since this spectrum determines the width of the α distribution. In general, all these discrepancies tend to be consistent with the observations made in the ATLAS $\gamma\gamma \to \mu^+\mu^-$ measurement [16], where the STARLIGHT predictions were found to underestimate the measured integrated fiducial cross-sections by about 10%.

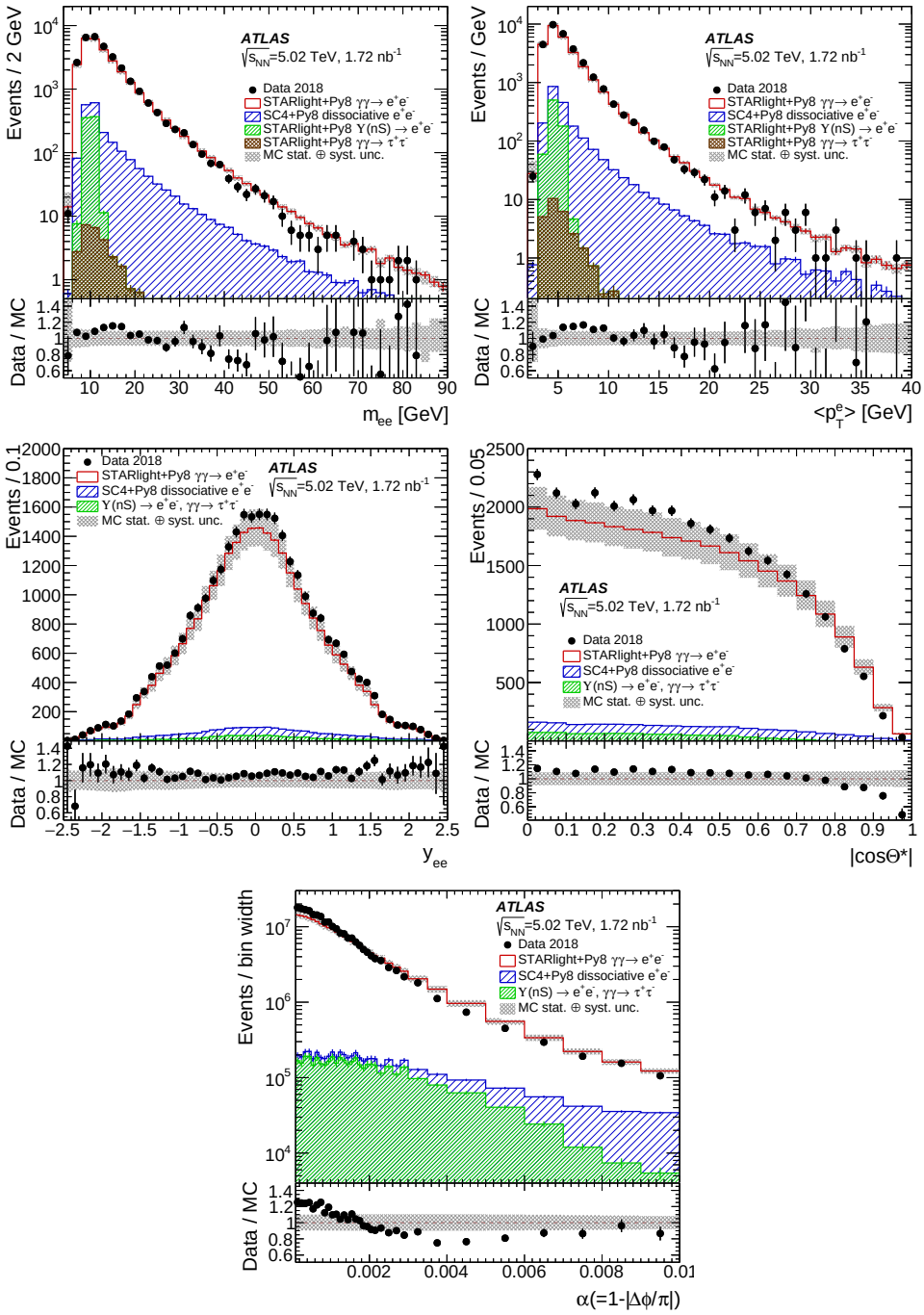

Figure 4: Distributions of m_{ee} (top left), $\langle p_{\mathrm{T}}^{e} \rangle$ (top right), y_{ee} (middle left), $|\cos\theta^{*}|$ (middle right), and α (bottom) for the inclusive sample in data and the MC predictions for signal and background processes. The lower panels show the ratio of data to MC simulation. Error bars represent statistical uncertainties. The shaded area represents the overall uncertainty of the total MC prediction. In the y_{ee}, $|\cos\theta^{*}|$, and α distributions, the Υ and $\tau^{+}\tau^{-}$ contributions are shown together. The dissociative contribution is scaled to constitute the f_{diss} fraction from the data fit.

6 Analysis

The integrated fiducial cross-section for exclusive dielectron production is calculated using the following formula:

$$\sigma^{\text{fid}} = \frac{N_{\text{data}} - N_{\text{bkg}}}{C \cdot A \cdot L},$$

where:

- N_{data} and N_{bkg} refer to the number of events in data after event selection and the expected number of background events in this selected sample, respectively;
- C is a correction factor accounting for detector inefficiencies (including the trigger), calculated as $N^{\text{fid,cut}}_{\text{MC,reco}}/N^{\text{fid,cut}}_{\text{MC,gen}}$ where $N^{\text{fid,cut}}_{\text{MC,gen}}$ is the number of generated events passing fiducial requirements of the analysis, while $N^{\text{fid,cut}}_{\text{MC,reco}}$ is the number of simulated signal events that also pass the reconstruction-level selection;
- A is the acceptance correction, used to correct the result for the exclusion of the calorimeter transition region and extrapolation from $|\eta^e| < 2.47$ to $|\eta^e| < 2.5$; and is calculated as $N^{\text{fid,cut}}_{\text{MC,gen}}/N^{\text{fid}}_{\text{MC,gen}}$, where $N^{\text{fid}}_{\text{MC,gen}}$ is the number of generated events passing all fiducial requirements of the analysis, except the requirement to exclude the calorimeter transition region;
- L is the total integrated luminosity.

Both $N^{\text{fid,cut}}_{\text{MC,gen}}$ and $N^{\text{fid}}_{\text{MC,gen}}$ are extracted with respect to the generator-level electrons before FSR. The fiducial region is defined by the following requirements: $p^e_{\text{T}} > 2.5\,\text{GeV}$, $|\eta^e| < 2.5$, $m_{ee} > 5\,\text{GeV}$, and $p^{ee}_{\text{T}} < 2\,\text{GeV}$. The number of events passing the fiducial selection is $N_{\text{data}} = 30456$. The dissociative and $\tau^+\tau^-$ background fraction obtained from the fit amounts to 4.5%. The Υ background amounts to 2.4% of all events satisfying the selection criteria.

The selected data sample is corrected in a few subsequent steps in order to compare it with the theoretical predictions. In the first step the backgrounds are subtracted. Distributions in the data are reweighted event-by-event by the factor $(1 - f_{\text{bkg}})$ where f_{bkg} is the fraction of background (inclusive in ZDC) from the fit in a given m_{ee} and $|y_{ee}|$ range. For masses above 40 GeV, the fraction obtained from the fit in the full $|y_{ee}| < 2.4$ range is taken. For events with m_{ee} below 40 GeV, the fraction as a function of $|y_{ee}|$ is used. If $|y_{ee}|$ exceeds 2.4, the fraction from the $1.6 < |y_{ee}| < 2.4$ bin is applied. In the next step, the background expected from $\Upsilon(nS)$ decays is subtracted.

For differential cross-section measurement, the data are corrected with fiducial correction factors defined as the fraction of events in each bin which fall into the fiducial region at generator level. These factors correct for the events that are reconstructed within the fiducial region, but fall outside it at the generator level. They are parameterised using the reconstructed kinematic variables. They deviate from unity at the subpercent level, so their impact is marginal. After this, the reconstructed data are unfolded using a Bayesian-inspired iterative procedure [42] with one iteration for all distributions implemented in the RooUnfold package [43], using response matrices derived from signal MC samples. The number of iterations is chosen to minimise the resulting statistical uncertainty and at the same time provide good closure. A closure test based on the signal MC samples is performed to validate the unfolding procedure. The signal sample is split into two parts. The first part is used to fill the response matrices, while the second one is unfolded. The ratio of the unfolded yields to the generated yields deviates from unity by 1% at most.

Finally, the distributions are divided by the luminosity as well as the product of correction factors, $C \times A$, which account for detector inefficiencies as well as acceptance losses. They are determined for each bin of the unfolded distribution as the fraction of events that pass the fiducial requirements at reconstruction level, in events that pass them at generator level. The $C \times A$ factors are parameterised using generator-level kinematics, but then weighted by trigger and reconstruction efficiency scale factors, evaluated at reconstruction level. The average C and A factors amount to 0.087 and 0.878, respectively.

7 Systematic uncertainties

The following systematic uncertainties are considered in the cross-section measurement. The total scale factors for the electron reconstruction and identification efficiency [38] are varied upwards and downwards coherently over the full kinematic range, as a conservative estimate. The data-driven trigger efficiency, which is the product of the L1 efficiency, the Pixel-veto efficiency, and the forward transverse energy requirement efficiency, is increased and decreased by its total uncertainty. To assess known uncertainties in the EM energy scale and energy resolution, the calibrations are varied by factors determined in 13 TeV pp collisions [38]. The background contributions are increased and decreased by their total uncertainties. The dissociative backgrounds are dominated by their statistical uncertainties from the fit. The systematic uncertainties are also evaluated, and the largest contribution is related to the shape of the signal template. This is estimated using data from the 0n0n category as a signal distribution for the Xn0n and XnXn categories. The background template shape uncertainty is estimated by adding the double dissociative component. The uncertainty in the expected Υ yields is dominated by both the efficiency scale factors and the EM energy scale. Given the small contribution from Υ production, the theoretical uncertainties of its cross-section are considered to have negligible impact on the final measurement.

For the differential cross-sections, additional systematic uncertainties are related to the unfolding procedures. The MC sample is split in two, with one subsample used to determine the response matrix and the other treated as a simulated data set. The differences between the generated and unfolded yields are treated as a systematic uncertainty. Similarly, the sensitivity to the Bayesian prior is tested by reweighting the simulated data set to agree with the reconstructed data. Again, the differences between simulated and reconstructed yields in this closure test are applied as an uncertainty. While the primary unfolding is evaluated in one dimension rather than two, a cross-check is performed using the response in two dimensions. For each of the unfolded variables, every other one is used in the second dimension, but with the number of bins reduced to four (three) for m_{ee} and $\langle p_{\mathrm{T}}^{e} \rangle$ ($|y_{ee}|$ and $|\cos\theta^{*}|$) to compensate for the limited number of events in the MC sample. The three resulting two-dimensional cross-sections are projected to one dimension and compared with the nominal results for each unfolded variable. The largest variations in each bin are included as an uncertainty. Finally, the spectra are evaluated in the 0n0n category, using the fractions determined in Section 4, but evaluated for generator-level m_{ee} and $|y_{ee}|$ (as opposed to the reconstructed values). The differences are found to be within 1%–2%.

The uncertainty in the integrated luminosity of the data sample is 2.0%. It is derived from the calibration of the luminosity scale using x–y beam-separation scans, following a methodology similar to that detailed in Ref. [44], and using the LUCID-2 detector for the baseline luminosity measurements [45].

A summary of the systematic uncertainties as a function of m_{ee} and $|y_{ee}|$ is shown in Figure 5. The dominant source of uncertainty arises from the uncertainties in the electron scale factors. They are at the level of 10%–11% in the whole range of m_{ee}, and rise from 9% at $|y_{ee}| \approx 0$ to about 15% for $|y_{ee}|$ close to 2. The systematic uncertainty from the trigger efficiency is approximately 2% for m_{ee} above 10 GeV and

$|y_{ee}|$ below 1.6. It rises to 4% for smaller m_{ee}, and to 6% for the highest $|y_{ee}|$ values. The uncertainty related to the energy scale and resolution is below 1% in the whole range of $|y_{ee}|$, but exceeds this value in some m_{ee} bins, reaching approximately 5% for the lowest m_{ee} values. The background uncertainties are within 1%–3% and increase slightly with increasing m_{ee} and $|y_{ee}|$. Uncertainties related to unfolding procedures do not exhibit such clear dependencies in m_{ee} and $|y_{ee}|$. They are mostly within the 2%–3% range but exceed this value, up to 5%, at intermediate m_{ee} and $|y_{ee}|$.

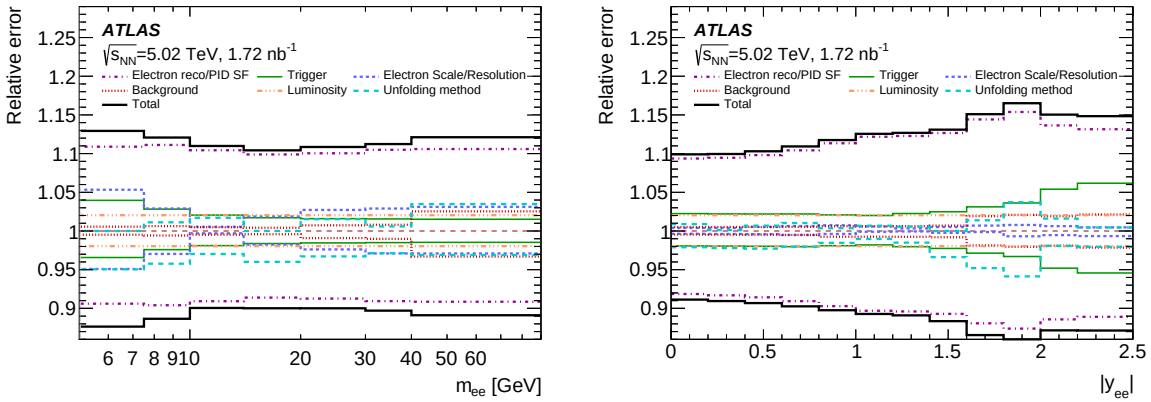

Figure 5: Breakdown of relative systematic uncertainties in the differential cross-section as a function of m_{ee} (left) and $|y_{ee}|$ (right).

8 Results

The total integrated fiducial cross-section is measured to be $215 \pm 1(\text{stat.}) \,^{+23}_{-20}(\text{syst.}) \pm 4(\text{lumi.})\,\mu$b. The STARLIGHT prediction for the total integrated fiducial cross-section is 196.9 μb, while the SUPERCHIC prediction is 235.1 μb. Both predictions are statistically compatible with the measurement.

The differential cross-sections for exclusive dielectron production are presented as a function of m_{ee}, $\langle p_{\mathrm{T}}^{e} \rangle$, $|y_{ee}|$, and $|\cos\theta^{*}|$ in Figure 6. The cross-sections are measured inclusively in the ZDC categories. The results are corrected for detector inefficiency and resolution effects, and are compared with STARLIGHT v3.13 and SUPERCHIC v3.05 predictions for the signal $\gamma\gamma \to e^{+}e^{-}$ process. The bottom panel in each plot shows the ratio of the unfolded data to MC predictions. On average the STARLIGHT predictions underestimate the data by about 10%–15%, while SUPERCHIC predictions are higher by about the same amount. The STARLIGHT and SUPERCHIC predictions tend to have very similar shapes. The difference in the absolute normalisation of the two predictions is due to different approaches in the implementation of the non-hadronic overlap condition of the Pb ions. The predictions describe the shape of the data well, except at high $|y_{ee}|$ and high $|\cos\theta^{*}|$. The differences are more pronounced for m_{ee} between 10 and 20 GeV, and for $\langle p_{\mathrm{T}}^{e} \rangle$ between 5 and 10 GeV. The ratio of data to STARLIGHT rises from about 1.1 to 1.2 as $|y_{ee}|$ increases from 0 to 2.5. For $|\cos\theta^{*}|$ close to 0, the data-to-STARLIGHT ratio reaches its largest value, around 1.15, and then slowly decreases to about 1.05 for $|\cos\theta^{*}| = 0.8$. The ratio falls more steeply in the last two bins of $|\cos\theta^{*}|$ and drops below unity to 0.75 and 0.65 for STARLIGHT and SUPERCHIC respectively. The measured cross-section in the highest $|\cos\theta^{*}|$ bin is 1.8 (2.7) standard deviations below the theory prediction from STARLIGHT (SUPERCHIC). There is a plausible proposal that higher-order scattering processes (involving

more than two photons in the initial state) are relevant and would tend to reduce the predicted cross-sections by the observed discrepancies [46].

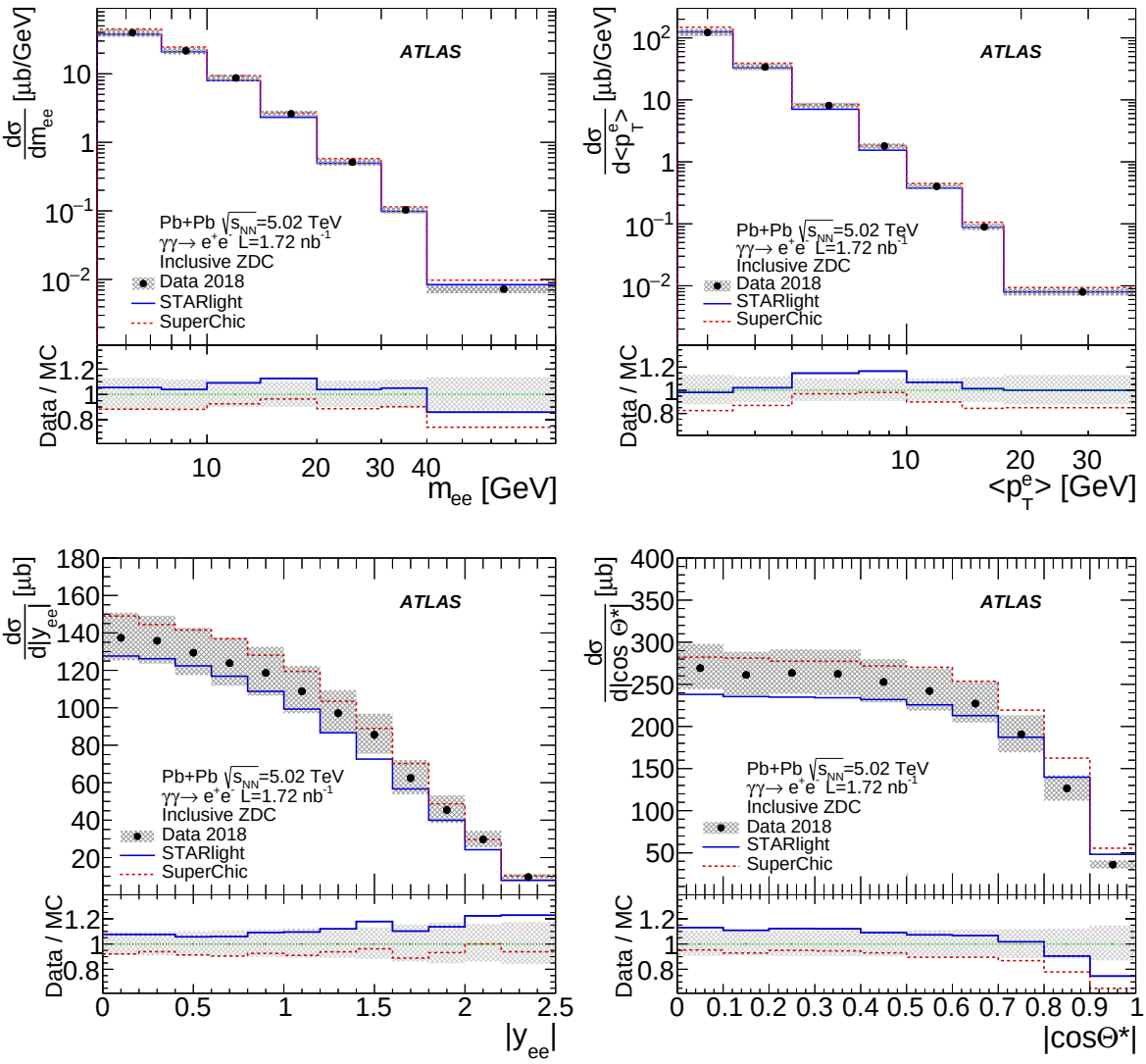

Figure 6: Fully corrected differential cross-sections measured inclusively in ZDC categories for exclusive dielectron production, $\gamma\gamma \to e^+e^-$, as a function of m_{ee}, $\langle p_T^e \rangle$, $|y_{ee}|$ and $|\cos\theta^*|$ for data (dots) and MC predictions from STARLIGHT (solid blue) and SUPERCHIC (dashed red). Bottom panels present the ratios of data to MC predictions. The shaded area represents the total uncertainty of the data, excluding the 2% luminosity uncertainty.

The differential cross-sections as a function of m_{ee}, $\langle p_T^e \rangle$, $|y_{ee}|$ and $|\cos\theta^*|$ for the 0n0n category are presented in Figure 7. They are compared with the MC predictions from STARLIGHT v3.13 and SUPERCHIC v3.05. Both simulated samples were produced inclusively and reweighted to the 0n0n category using the measured fractions in the inclusive data sample. Each theory prediction is represented by two curves reflecting the systematic variations of the measured 0n0n fractions. STARLIGHT can also generate a prediction conditional on the presence of neutron emission in one or both directions. These dedicated predictions from STARLIGHT for the 0n0n category are shown in the same plots. That prediction agrees well

with the shape of the inclusive STARLIGHT prediction corrected for the measured 0n0n fractions, but is systematically lower by 2%–3% for $|y_{ee}| < 1.4$. The general conclusions from this comparison between MC predictions and data are consistent with the inclusive case. Agreement between data and MC events is generally better for lower $|y_{ee}|$ and $|\cos\theta^*|$ values, i.e. involving lower-energy initial-state photons.

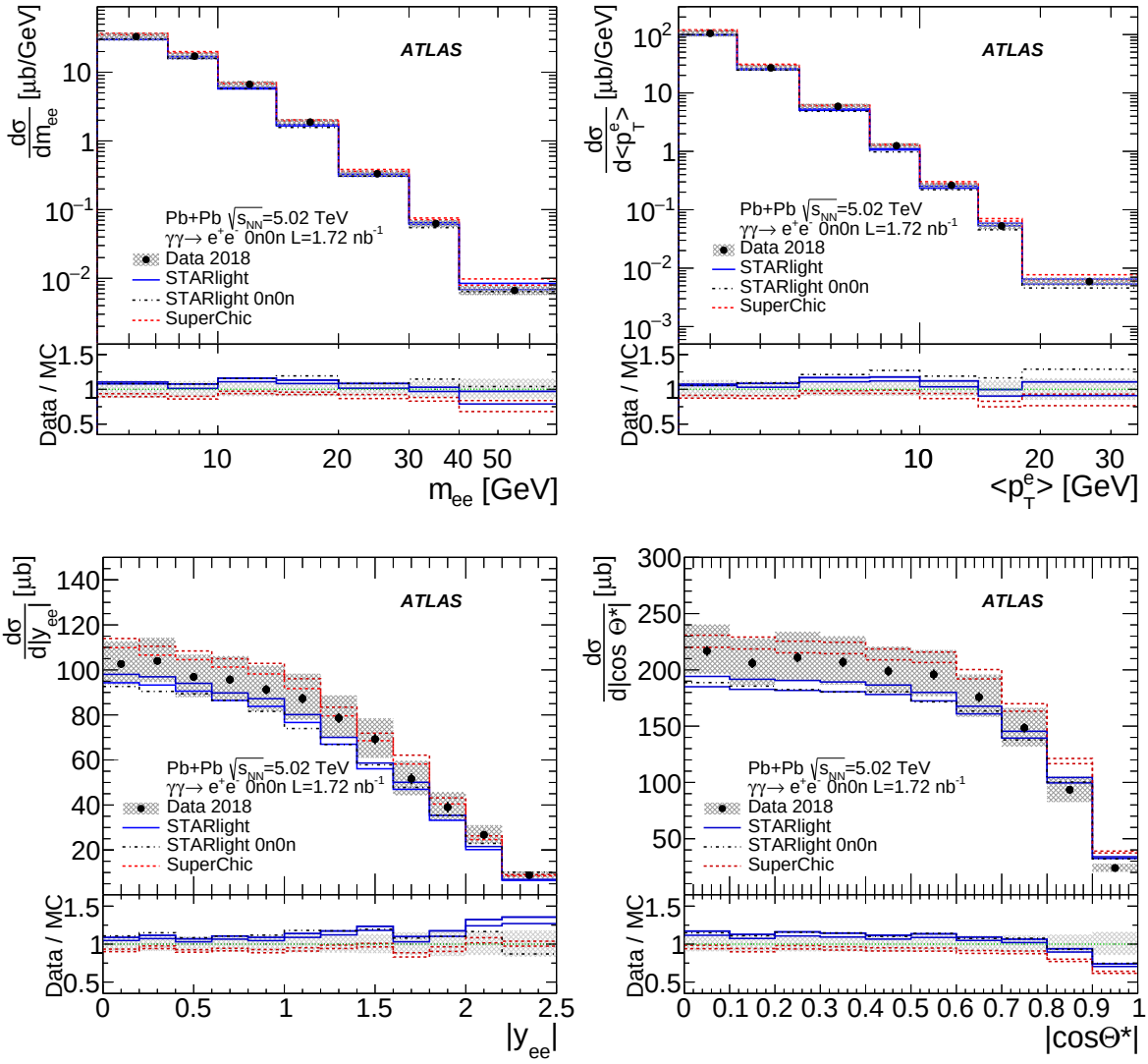

Figure 7: Fully corrected differential cross-sections measured for the 0n0n category for exclusive dielectron production as a function of m_{ee}, $\langle p_{\mathrm{T}}^{e}\rangle$, $|y_{ee}|$ and $|\cos\theta^*|$. The cross-sections are compared with MC predictions from STARLIGHT (solid blue) and SUPERCHIC v3.05 (dashed red), each represented by two lines reflecting systematic variations. Also, a dedicated prediction from STARLIGHT for the 0n0n category (dashed-dotted black) is shown. The bottom panels show the ratios of data to predictions. The shaded area represents the total uncertainty of the data, excluding the 2% luminosity uncertainty.

9 Conclusions

A measurement of the cross-section for exclusive dielectron production, $\gamma\gamma \to e^+e^-$, is performed using $\mathcal{L}_{\text{int}} = 1.72\ \text{nb}^{-1}$ of ultraperipheral Pb+Pb collision data at $\sqrt{s_{\text{NN}}} = 5.02\,\text{TeV}$ recorded by the ATLAS detector at the LHC. The cross-section is corrected for detector efficiency, acceptance losses, and background contributions. The backgrounds from dissociative processes, Υ decays, and $\tau^+\tau^-$ production are subtracted, with the first contribution estimated using a template fit to the acoplanarity distribution. After all corrections, the integrated cross-section for the $\gamma\gamma \to e^+e^-$ process in the fiducial region, defined by $p_{\text{T}}^e > 2.5\,\text{GeV}$, $|\eta^e| < 2.5$, $m_{ee} > 5\,\text{GeV}$, and $p_{\text{T}}^{ee} < 2\,\text{GeV}$ requirements, is measured to be $215 \pm 1(\text{stat.})\ ^{+23}_{-20}(\text{syst.}) \pm 4(\text{lumi.})\ \mu\text{b}$. Within experimental uncertainties the data are in good agreement with the QED predictions from Starlight v3.13 and SuperChic v3.05. The differential cross-sections are presented as a function of m_{ee}, $\langle p_{\text{T}}^e \rangle$, $|y_{ee}|$ and $|\cos\theta^*|$, both with and without requirements on forward neutron activity. The differential results are compared with the predictions from Starlight v3.13 and SuperChic v3.05. In general, the shapes of the distributions agree well, but some systematic differences are observed. In particular, the discrepancy between data and the Starlight prediction rises with higher $|y_{ee}|$, similarly to what ATLAS observed previously in $\gamma\gamma \to \mu^+\mu^-$ production. For $|\cos\theta^*| \approx 1$, the measured cross-section is 1.8 (2.7) standard deviations below the theory prediction from Starlight (SuperChic). Agreement between data and MC simulation is generally better for lower $|y_{ee}|$ and $|\cos\theta^*|$ values.

References

[1] A. J. Baltz et al., *The physics of ultraperipheral collisions at the LHC*, Phys. Rep. **458** (2008) 1, ISSN: 0370-1573, URL: https://www.sciencedirect.com/science/article/pii/S0370157307004462.

[2] S. R. Klein and P. Steinberg, *Photonuclear and Two-photon Interactions at High-Energy Nuclear Colliders*, Ann. Rev. Nucl. Part. Sci. **70** (2020) 323, arXiv: 2005.01872 [nucl-ex].

[3] E. Fermi, *On the theory of collisions between atoms and electrically charged particles*, Nuovo Cim. **2** (1925) 143, arXiv: hep-th/0205086 [hep-th].

[4] E. J. Williams, *Nature of the High Energy Particles of Penetrating Radiation and Status of Ionization and Radiation Formulae*, Phys. Rev. **45** (1934) 729.

[5] G. Breit and J. A. Wheeler, *Collision of Two Light Quanta*, Phys. Rev. **46** (1934) 1087.

[6] A. Veyssiere, H. Beil, R. Bergere, P. Carlos and A. Lepretre, *Photoneutron cross sections of ^{208}Pb and ^{197}Au*, Nucl. Phys. A **159** (1970) 561, ISSN: 0375-9474, URL: https://www.sciencedirect.com/science/article/pii/037594747090727X.

[7] ATLAS Collaboration, *Measurement of exclusive $\gamma\gamma \to \ell^+\ell^-$ production in proton-proton collisions at $\sqrt{s} = 7$ TeV with the ATLAS detector*, Phys. Lett. B **749** (2015) 242, arXiv: 1506.07098 [hep-ex].

[8] CMS Collaboration, *Search for Exclusive or Semi-Exclusive Photon Pair Production and Observation of Exclusive and Semi-Exclusive Electron Pair Production in pp Collisions at $\sqrt{s} = 7$ TeV*, JHEP **11** (2012) 080, arXiv: 1209.1666 [hep-ex].

[9] CMS Collaboration, *Exclusive photon-photon production of muon pairs in proton-proton collisions at $\sqrt{s} = 7$ TeV*, JHEP **01** (2012) 052, arXiv: 1111.5536 [hep-ex].

[10] ATLAS Collaboration, *Measurement of the exclusive $\gamma\gamma \to \mu^+\mu^-$ process in proton-proton collisions at $\sqrt{s} = 13$ TeV with the ATLAS detector*, Phys. Lett. B **777** (2018) 303, arXiv: 1708.04053 [hep-ex].

[11] ATLAS Collaboration, *Observation and Measurement of Forward Proton Scattering in Association with Lepton Pairs Produced via the Photon Fusion Mechanism at ATLAS*, Phys. Rev. Lett. **125** (2020) 261801, arXiv: 2009.14537 [hep-ex].

[12] CMS and TOTEM Collaborations, *Observation of proton-tagged, central (semi)exclusive production of high-mass lepton pairs in pp collisions at 13 TeV with the CMS-TOTEM precision proton spectrometer*, JHEP **07** (2018) 153, arXiv: 1803.04496 [hep-ex].

[13] ALICE Collaboration, *Charmonium and e^+e^- pair photoproduction at mid-rapidity in ultra-peripheral Pb-Pb collisions at $\sqrt{s_{\rm NN}}$=2.76 TeV*, Eur. Phys. J. C **73** (2013) 2617, arXiv: 1305.1467 [nucl-ex].

[14] STAR Collaboration, *Low-p_T e^+e^- pair production in Au+Au collisions at $\sqrt{s_{NN}} = 200$ GeV and U+U collisions at $\sqrt{s_{NN}} = 193$ GeV at STAR*, Phys. Rev. Lett. **121** (2018) 132301, arXiv: 1806.02295 [hep-ex].

[15] STAR Collaboration, *Measurement of e^+e^- Momentum and Angular Distributions from Linearly Polarized Photon Collisions*, Phys. Rev. Lett. **127** (2021) 052302, arXiv: 1910.12400 [nucl-ex].

[16] ATLAS Collaboration,
Exclusive dimuon production in ultraperipheral Pb+Pb collisions at $\sqrt{s_{\mathrm{NN}}}$ = 5.02 TeV with ATLAS, Phys. Rev. C **104** (2021) 024906, arXiv: 2011.12211 [nucl-ex].

[17] ATLAS Collaboration, *Observation of centrality-dependent acoplanarity for muon pairs produced via two-photon scattering in Pb+Pb collisions at $\sqrt{s_{\mathrm{NN}}}$ = 5.02 TeV with the ATLAS detector*, Phys. Rev. Lett. **121** (2018) 212301, arXiv: 1806.08708 [nucl-ex].

[18] CMS Collaboration, *Observation of Forward Neutron Multiplicity Dependence of Dimuon Acoplanarity in Ultraperipheral Pb-Pb Collisions at $\sqrt{s_{NN}}$=5.02 TeV*, Phys. Rev. Lett. **127** (2021) 122001, arXiv: 2011.05239 [hep-ex].

[19] M. Dyndał, M. Kłusek-Gawenda, A. Szczurek and M. Schott, *Anomalous electromagnetic moments of τ lepton in $\gamma\gamma \to \tau^+\tau^-$ reaction in Pb+Pb collisions at the LHC*, Phys. Lett. B **809** (2020) 135682, ISSN: 0370-2693.

[20] L. Beresford and J. Liu, *New physics and tau $g-2$ using LHC heavy ion collisions*, Phys. Rev. D **102** (2020) 113008,
URL: https://link.aps.org/doi/10.1103/PhysRevD.102.113008.

[21] ATLAS Collaboration,
Evidence for light-by-light scattering in heavy-ion collisions with the ATLAS detector at the LHC, Nature Phys. **13** (2017) 852, arXiv: 1702.01625 [hep-ex].

[22] ATLAS Collaboration, *Observation of light-by-light scattering in ultraperipheral Pb+Pb collisions with the ATLAS detector*, Phys. Rev. Lett. **123** (2019) 052001, arXiv: 1904.03536 [hep-ex].

[23] ATLAS Collaboration, *Measurement of light-by-light scattering and search for axion-like particles with 2.2 nb^{-1} of Pb+Pb data with the ATLAS detector*, JHEP **11** (2021) 050,
arXiv: 2008.05355 [hep-ex].

[24] CMS Collaboration, *Evidence for light-by-light scattering and searches for axion-like particles in ultraperipheral PbPb collisions at $\sqrt{s_{\mathrm{NN}}}$ = 5.02 TeV*, Phys. Lett. B **797** (2019) 134826,
arXiv: 1810.04602 [hep-ex].

[25] ATLAS Collaboration, *The ATLAS experiment at the CERN Large Hadron Collider*, JINST **3** (2008) S08003.

[26] ATLAS Collaboration, *ATLAS Insertable B-Layer Technical Design Report*, (2010),
URL: https://cds.cern.ch/record/1291633.

[27] ATLAS Collaboration, *Performance of the ATLAS Trigger System in 2015*, Eur. Phys. J. C **77** (2017) 317, arXiv: 1611.09661 [hep-ex].

[28] ATLAS Collaboration, *Operation of the ATLAS trigger system in Run 2*, JINST **15** (2020) P10004,
arXiv: 2007.12539 [hep-ex].

[29] ATLAS Collaboration, *The ATLAS Collaboration Software and Firmware*,
ATL-SOFT-PUB-2021-001, 2021, URL: https://cds.cern.ch/record/2767187.

[30] ATLAS Collaboration, *ATLAS data quality operations and performance for 2015–2018 data-taking*, JINST **15** (2020) P04003, arXiv: 1911.04632 [physics.ins-det].

[31] S. R. Klein, J. Nystrand, J. Seger, Y. Gorbunov and J. Butterworth, *STARlight: A Monte Carlo simulation program for ultra-peripheral collisions of relativistic ions*, Comput. Phys. Commun. **212** (2017) 258, arXiv: 1607.03838 [hep-ph].

[32] M. L. Miller, K. Reygers, S. J. Sanders and P. Steinberg, *Glauber Modeling in High-Energy Nuclear Collisions*, Ann. Rev. Nucl. Part. Sci. **57** (2007) 205, URL: https://doi.org/10.1146/annurev.nucl.57.090506.123020.

[33] L. A. Harland-Lang, V. A. Khoze and M. G. Ryskin, *Exclusive LHC physics with heavy ions: SuperChic 3*, Eur. Phys. J. C **79** (2019) 39, URL: https://doi.org/10.1140/epjc/s10052-018-6530-5.

[34] T. Sjöstrand et al., *An introduction to PYTHIA 8.2*, Comput. Phys. Commun. **191** (2015) 159, arXiv: 1410.3012 [hep-ph].

[35] L. A. Harland-Lang, M. Tasevsky, V. A. Khoze and M. G. Ryskin, *A new approach to modelling elastic and inelastic photon-initiated production at the LHC: SuperChic 4*, Eur. Phys. J. C **80** (2020) 925, arXiv: 2007.12704 [hep-ph].

[36] ATLAS Collaboration, *The ATLAS Simulation Infrastructure*, Eur. Phys. J. C **70** (2010) 823, arXiv: 1005.4568 [physics.ins-det].

[37] GEANT4 Collaboration, S. Agostinelli et al., *GEANT4: A Simulation toolkit*, Nucl. Instrum. Meth. A **506** (2003) 250.

[38] ATLAS Collaboration, *Electron and photon performance measurements with the ATLAS detector using the 2015–2017 LHC proton-proton collision data*, JINST **14** (2019) P12006, arXiv: 1908.00005 [hep-ex].

[39] ATLAS Collaboration, *Early Inner Detector Tracking Performance in the 2015 Data at $\sqrt{s}$ = 13 TeV*, ATL-PHYS-PUB-2015-051, 2015, URL: https://cds.cern.ch/record/2110140.

[40] ATLAS Collaboration, *Performance of the ATLAS track reconstruction algorithms in dense environments in LHC Run 2*, Eur. Phys. J. C **77** (2017) 673, arXiv: 1704.07983 [hep-ex].

[41] ALICE Collaboration, B. Abelev et al., *Measurement of the Cross Section for Electromagnetic Dissociation with Neutron Emission in Pb-Pb Collisions at $\sqrt{s_{NN}}$ = 2.76 TeV*, Phys. Rev. Lett. **109** (2012) 252302, arXiv: 1203.2436 [nucl-ex].

[42] G. D'Agostini, *A multidimensional unfolding method based on Bayes' theorem*, Nucl. Instrum. Meth. A **362** (1995) 487, ISSN: 0168-9002, URL: https://www.sciencedirect.com/science/article/pii/016890029500274X.

[43] T. Adye, 'Unfolding algorithms and tests using RooUnfold', *Proceedings, 2011 Workshop on Statistical Issues Related to Discovery Claims in Search Experiments and Unfolding (PHYSTAT 2011)* (CERN, Geneva, Switzerland, 17th–20th Jan. 2011) 313, arXiv: 1105.1160 [physics.data-an].

[44] ATLAS Collaboration, *Luminosity determination in pp collisions at $\sqrt{s}$ = 8 TeV using the ATLAS detector at the LHC*, Eur. Phys. J. C **76** (2016) 653, arXiv: 1608.03953 [hep-ex].

[45] G. Avoni et al., *The new LUCID-2 detector for luminosity measurement and monitoring in ATLAS*, JINST **13** (2018) P07017.

[46] W. Zha and Z. Tang,
Discovery of higher-order quantum electrodynamics effect for the vacuum pair production,
JHEP **08** (2021) 083, arXiv: 2103.04605 [hep-ph].